H4.SMR/1013-17

SCHOOL ON THE USE OF SYNCHROTRON RADIATION IN SCIENCE AND TECHNOLOGY:
"John Fuggle Memorial"

3 November - 5 December 1997

Miramare - Trieste, Italy

Fermi Surface Mapping by Photoemission

C. S. Fadley
Lawrence Berkeley Laboratory , California - USA

Fermi Surface Mapping by Photoemission*

J. Osterwalder, Physik-Institut, Universität Zürich-Irchel,
Winterthurerstr. 190, CH-8057 Zürich, Switzerland

Introduction

The shape and the volume of the Fermi surface of a metal is intimately related to many of its physical properties [1]. It is therefore not surprising that some of the first precise measurements of the electronic structure of metals were carried out at their Fermi surfaces using the de-Haas-van-Alphen (dHvA) and related effects where the oscillatory behaviour of some physical property, such as e.g. the magnetic susceptibility, is recorded as a function of the applied magnetic field. Extremal orbits on the Fermi surface within the plane perpendicular to the magnetic field direction are determined very accurately, and by combining the information on such orbits for many field orientations the whole Fermi surface can be reconstructed. Other Fermi surface probes have been developed since, using e.g. Compton scattering [2] or positron annihilation [3]. While these other techniques put much less stringent requirements on sample quality and temperature they offer relatively limited resolution in $\mathbf{k}$-space. All these methods are volume sensitive probes and provide no surface-related information.

In the meantime, angle-resolved ultraviolet photoelectron spectroscopy (ARUPS) has been developed into a powerful tool for studying occupied electronic bands also further away from the Fermi energy, providing both volume and surface sensitive information [4]. Early on, Fermi surface data from dHvA experiments were used for calibrating the absolute $\mathbf{k}$-locations of certain bands crossing the Fermi level. This calibration was found necessary as the photoelectron carries direct information on $\mathbf{k}_{\parallel}$, the $\mathbf{k}$-component parallel to the surface, while its normal component $\mathbf{k}_{\perp}$ is affected by the surface potential energy step, by details of the final-state dispersion relation $E(\mathbf{k})$, and by the smearing associated with the short photoelectron escape depth [4]. On the other hand, it was soon realized that this technique provided access to the complete band structure, including the Fermi surface, of two-dimensional (2D) systems, including surface states, where $\mathbf{k}_{\parallel}$ is the relevant quantum number. These latter experiments locate Fermi level crossings of energy bands in measured angle-resolved energy spectra in order to trace Fermi surface contours [5]. Alternatively, a few groups have recently begun to map Fermi surfaces by measuring intensities of photoelectrons emitted from the Fermi edge as a function of emission angles relative to the crystal axes [6-12] and thus as a function of $\mathbf{k}_{\parallel}$. In principle, the two experimental procedures for locating Fermi surface contours are equivalent: At those $\mathbf{k}_{\parallel}$ positions where a

band crosses the Fermi level, the photoemission intensity at the Fermi level rises sharply, contributing to the measured contour in the intensity map.

In this lecture this latter experimental technique will be introduced. The important test case of copper will be discussed, providing a simple and intuitive connection between the measured 2D contours and the well-known Fermi surface of three-dimensional (3D) copper. Recent measurements on ferromagnetic nickel will be given and compared with Fermi surface data from dHvA experiments. Applications to 2D systems include high-temperature superconductors, where the relevant conduction electrons are quasi-2D, and sp-derived surface states on Cu and Al surfaces.

Angle-Resolved Photoemission

The theory of angle-resolved photoemission has been excellently reviewed by Hüfner [4]. We limit our discussion here to a few simple concepts that are necessary in order to intuitively understand the Fermi surface mapping experiments. For conceptual simplicity we shall remain within the so-called three-step model, which describes the photoemission process as a sequence of - (i) the photoexcitation of a band electron into an empty band - (ii) the propagation of this excited electron to the surface and - (iii) the transmission of this electron through the surface into the vacuum. We make the approximation of a free electron final state to describe the photoexcited electron within the solid, which often is a good starting point for the interpretation of ARUPS data.

In the photoexcitation process (i) energy and crystal momentum are conserved. For a given photon energy $h\nu$ and for an initial state with wave vector k_i and energy $E_i(k_i)$ we thus have

$$E_f(k_f) = E_i(k_i) + h\nu \qquad (1)$$

and

$$k_f = k_i + k_{h\nu} + G. \qquad (2)$$

For photon energies cf the order of 20eV the associated photon wave vector $k_{h\nu}$ is not more than a percent of typical Brillouin zone (BZ) dimensions and can thus be neglected in Eq. (2). The 3D reciprocal lattice vector G is needed in order to provide the momentum for the electron to escape from the crystal. These conservation laws imply that the dominant emission features appear as vertical or direct transitions (DT) within the band structure of a solid, as is depicted in Fig. 1. If we now consider transitions from the Fermi surface only, we must find locations k_F where a band crosses the Fermi energy E_F, and which is separated vertically from some empty band by the photon energy used in the experiment. Fig. 1 illustrates how such locations can be conveniently found by viewing the initial state band, and thus the Fermi surface, in the repeated zone scheme and the free-electron final-state parabola in the extended zone scheme. The figure also makes clear that these conservation laws put rather stringent conditions on k and that they can
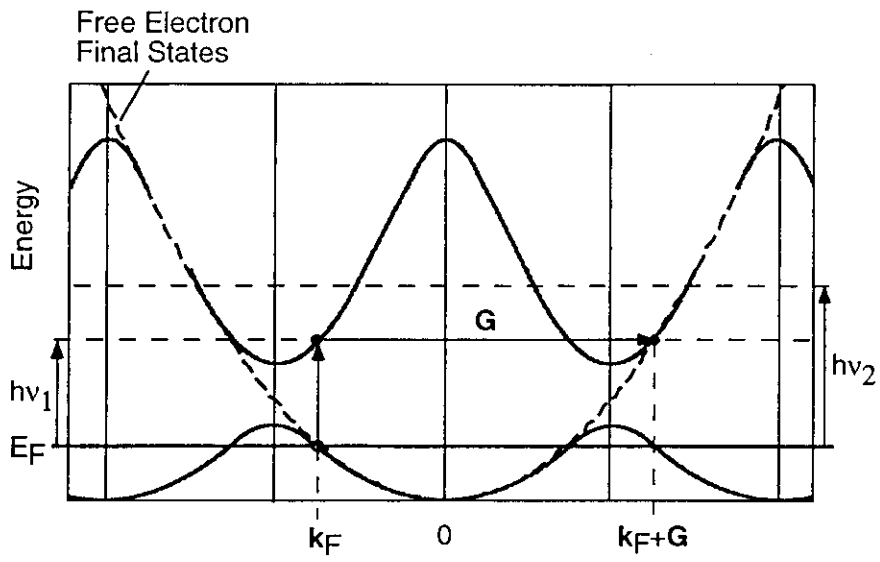
Fig. 1: Illustration of a direct transition (DT) from the Fermi surface of a solid. The band structure E(**k**) (solid curves) is given in the repeated zone scheme while the free-electron final state parabola (dashed curve) is drawn in the extended zone scheme. Along this particular direction of **k** there is a DT for the photon energy $h\nu_1$ and not for $h\nu_2$.
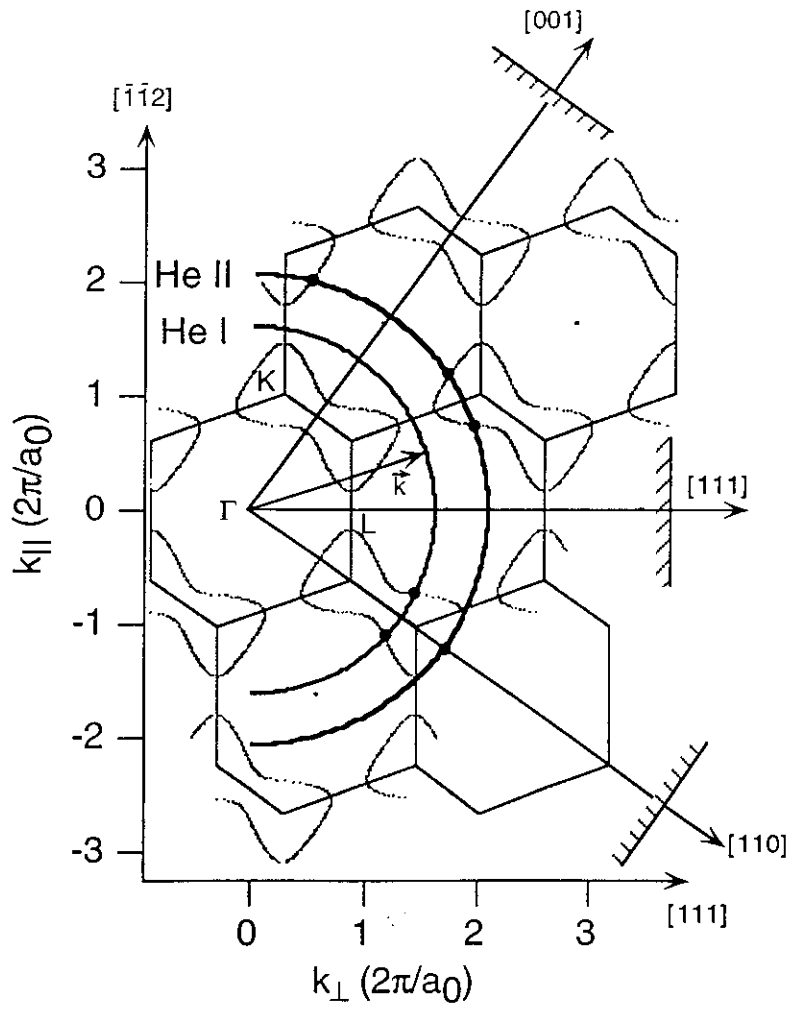

Fig. 2: High symmetry plane perpendicular to the [$\bar{1}$10] direction in the reciprocal lattice of copper. The solid polygons correspond to a section through the bulk Brillouin zones. Fermi surface sections are given by dotted curves. Large circles indicate free-electron final states for HeI and HeII radiation (21.2eV and 40.8eV, respectively). The orientation of three low-index surfaces is indicated.

be fulfilled only along few directions for a given photon energy. In order to provide an overview of where such transitions are to be expected in reciprocal space, Fig. 2 shows a planar section through k-space parallel to the ($\bar{1}$10) plane of the face-centered cubic lattice of copper and containing the origin Γ. Brillouin zones are indicated and the Fermi surface is given in the repeated zone scheme. The large circles give the possible free-electron wave vectors for the final-states associated with two different photon energies, specifically HeI (21.2 eV) and HeII (40.8 eV) radiation. According to Fig. 1 direct transitions occur at intersections of these spheres with the Fermi surface. Since the free-electron final state sphere and the Fermi surface represent intersecting hypersurfaces in 3D reciprocal space we expect these locations to be sets of continuous lines. Fig. 3 illustrates such a set of lines as one should observe for Fermi surface emission from a Cu(001) surface using HeI
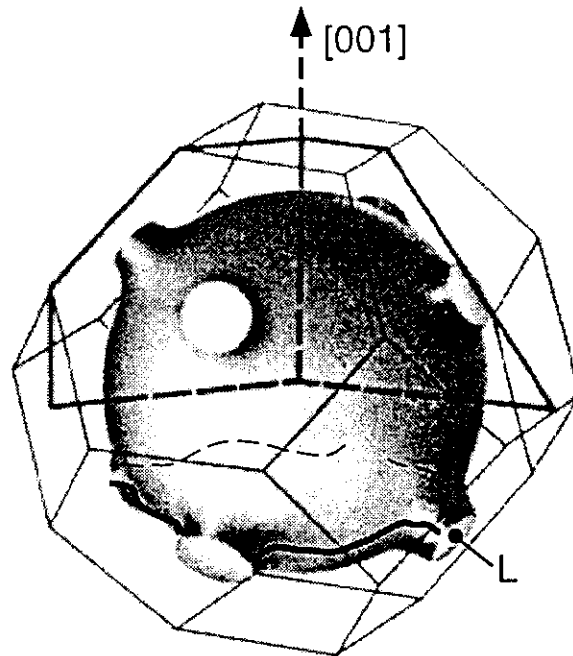

Fig. 3: 3D representation of the Fermi surface of copper, displaying the necks at equivalent L points. The solid and dashed curves near the bottom indicate the section measured at a photon energy of 21.2eV.

radiation. Within the ($\bar{1}$10) plane shown in Fig. 2, there is no intersection as the final state falls into the well-known necks associated with the zone boundaries near equivalent L points. However, for emission planes other than that a Fermi level crossing should be observed, thus giving a rounded-square-like Fermi contour, providing thus a direct mapping of the Fermi surface.

We neglect the scattering processes that the excited electrons undergo while propagating to the surface in step (ii). They affect essentially the transition intensities and widths and not their positions. On the other hand we have to consider the refraction effects due to the surface potential energy step (iii). For a given photon energy $h\nu$, the measured kinetic energy E_{kin}^{m} of the electrons emitted from the Fermi level is given by

$$E_{kin}^m = h\nu - \Phi \tag{3}$$

where Φ is the work function of the sample. Inside the solid the kinetic energy of the same electrons is higher by an amount given by the inner potential V_0, i.e. the average attractive potential due to the Coulomb interaction with the ion cores and the other valence electrons. We have thus

$$E_f(\mathbf{k}_f) = E_{kin}^m + V_0. \tag{4}$$

Assuming free-electron dispersion relations in both cases, i.e.

$$E_f(\mathbf{k}_f) = \frac{\hbar^2 k_f^2}{2m} \quad \text{and} \quad E_{kin}^m = \frac{\hbar^2 k_m^2}{2m}, \tag{5}$$

and considering the conservation of parallel momentum, one arrives at the equivalent of Snell's law of refraction (Fig. 4):

$$\sin\theta = \sin\theta_m \sqrt{\frac{h\nu - \Phi}{h\nu - \Phi + V_0}}. \tag{6}$$

Here, θ_m is the polar angle relative to the surface normal under which the photoelectrons are detected while θ is the internal polar angle of the same electrons prior to leaving the surface. Values for V_0 and Φ can be found in the
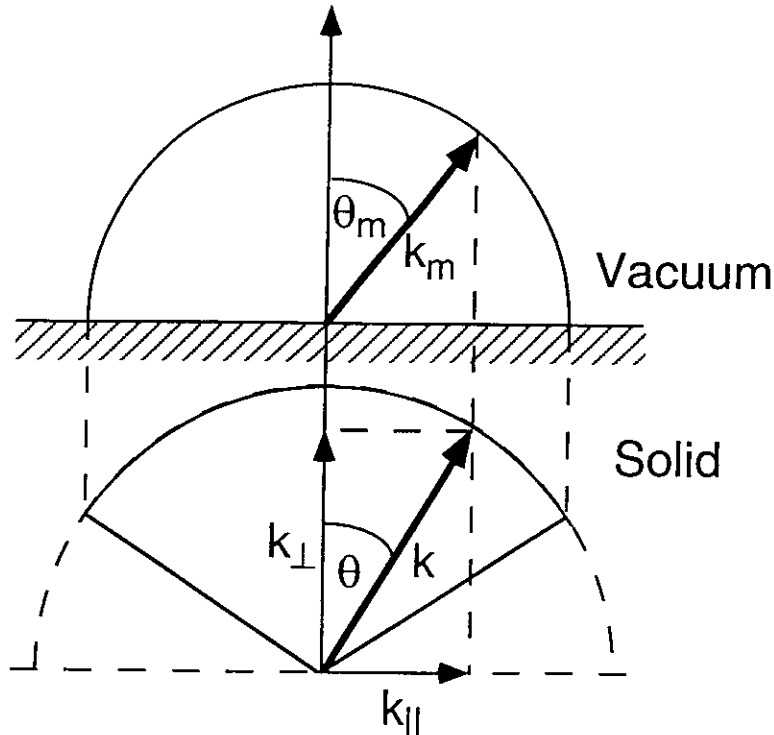

Fig. 4: Refraction at the surface potential step: Photoelectrons have longer wave vectors inside the solid (larger circle) than outside. For periodic surfaces $k_{\parallel}$ is strictly conserved.

literature for many crystal surfaces. By taking E_{kin}^{m} according to Eq. (3) and by defining the electron detection direction by the polar angle θ_m (Fig. 4) and the azimuthal angle ϕ_m one can thus determine, within this simplified model, absolute k-positions inside the solid:

$$k = \frac{1}{\hbar}\sqrt{2m(h\nu - \Phi + V_0)}(\sin\theta\cos\phi_m, \sin\theta\sin\phi_m, \cos\theta) \qquad (7)$$

where ϕ_m is usually measured relative to some high-symmetry direction of the crystal.

These concepts can be readily transposed to the case of a 2D system. In this case the initial states are defined by $k_\parallel$ while we consider the same 3D free-electron final states. Since $k_\parallel$ is conserved rigorously and since the final state can pick up any amount of $k_\perp$ needed from the underlying crystal - there is no quantization of $k_\perp$ for a 2D system - the same intuitive picture arises if the Fermi surface is viewed as a prismatic hypersurface in 3D k-space with the 2D Fermi surface as its base in the $k_\parallel$ plane (Fig. 5). Obviously, one can here map the entire Fermi surface out to the refraction-corrected free-electron sphere using a single photon energy, while one obtains only slices in the 3D case. However, using tunable synchrotron radiation for excitation, such slices can be measured for various sphere radii and the full Fermi surface can in principle be constructed also for a 3D crystal.
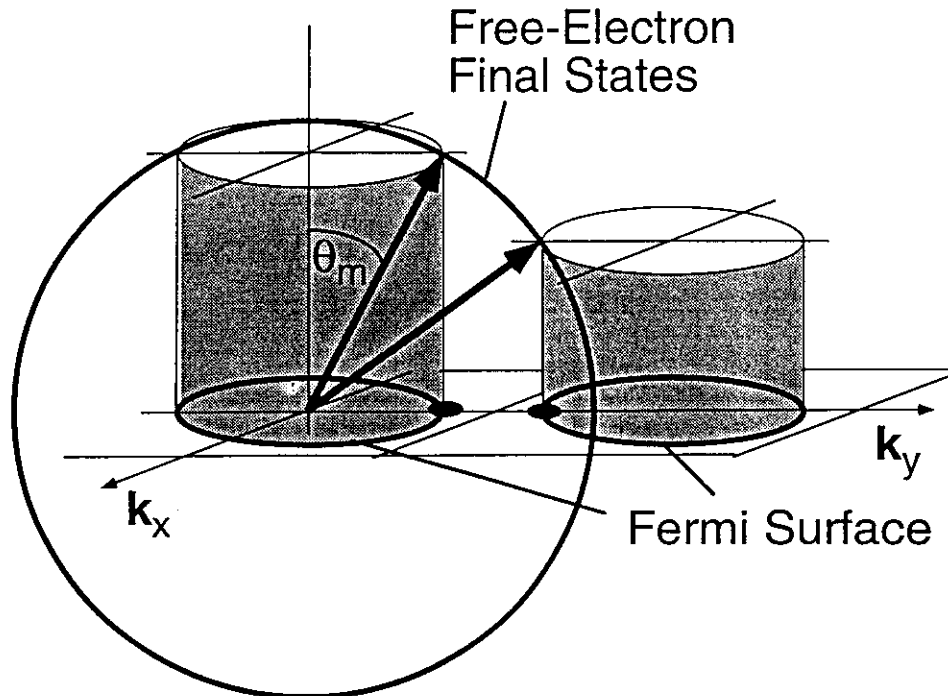

Fig. 5: Condition for the occurrence of a direct transition in k-space for a 2D system: The Fermi surface is represented by a prismatic hypersurface in 3D k-space. Free-electron final states are indicated by the solid circle.

Experimental Considerations

As outlined in the preceeding section, mapping a Fermi surface consists in finding all those **k**-vectors where direct transitions from the Fermi surface produce photoelectron intensities. In fact elastic and quasielastic electron-electron, electron-phonon and electron-defect scattering leads to non-**k**-conserving, so called non-direct transitions [13] that produce intensities also away from the direct transitions, though usually much weaker. For a fixed photon energy the detected electron emission direction is swept over a large part of the hemisphere above the surface while the emission intensity at the Fermi level is monitored. Two different experimental approaches have been followed for this procedure. In the first Fermi-surface mapping experiment presented by Santoni et al. [6], a display-type analyzer [14] was used for parallel detection of a large piece of solid angle. While this device permits a very efficient data collection with acquisition times of the order of a few minutes, it has certain limitations due to angular distortions, low signal-to-background ratios, detector inhomogeneities, and limited energy resolution by today's standards. The first three points make a set of careful calibration measurements necessary each time which reduces somewhat the efficiency of this approach.
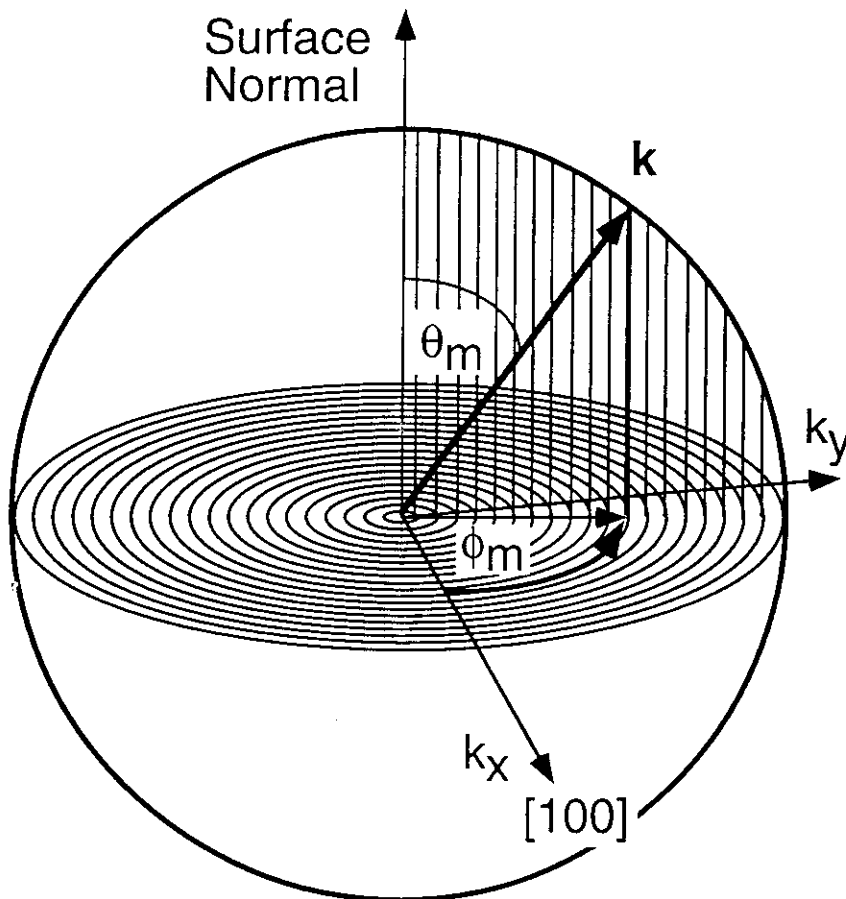

Fig. 6: Sequential angle-scanning mode for a mapping of $k_{||}$ with a uniform sampling density by crystal rotation. Scanning starts at grazing emission angles and proceeds in an azimuthal fashion up to the surface normal, covering several thousand angular settings.

More accurate measurements have been carried out using a sequential data acquisition of one angle at a time. In this case a highly optimized angle- and energy-resolving electron detector can be used. The setup used in the University of Fribourg laboratory, from which all the data presented in these notes are taken, has a geometry in which this analyzer sits fixed in space while the sample is rotated so as to cover all emission directions relative to the crystal axes. The angle scanning is done by computer controlled stepping motors that drive both a polar tilt axis and an azimuthal rotation of the sample about its normal. A sequence of azimuthal circles at decreasing polar angles (Fig. 6) has proven very successful, as each closing circle provides a consistency test for experimental stability and reproducibility [15]. A uniform sampling density in $k_{||}$ is achieved by varying the polar step size with $1/\cos\theta_m$ and by increasing azimuthal steps with decreasing polar angle. Typically more than 4000 angles are sampled and mapped onto $k_{||}$, with intensity values represented in a linear gray scale, with acquisition times being in the range of one up to several hours. Even though surface cleanliness is a concern with such measuring times, ultrahigh vacuum conditions in the low 10^{-11} mbar range have made it possible to study reactive systems such as Na layers on Al surfaces [16]. In this procedure the detection efficiency as well as the angular and energy resolution are completely uniform for the entire solid angle which is measured. Resolutions of $<1°$ in angle and ca. 30 meV in energy are routinely achieved. The He discharge lamp can be maintained at stable conditions to within 5% for extended measuring times. Due to the low background intensities and the constant detection efficiency even weak features on the Fermi surface can be observed.
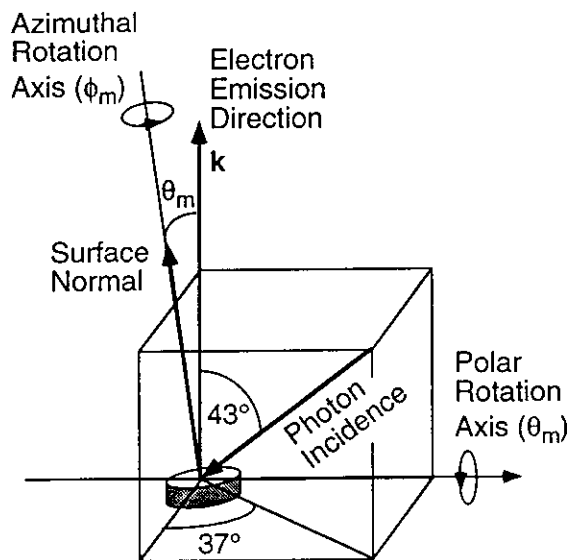

Fig. 7: Geometry of the experimental setup used for all data presented in these notes. Note that the photon incidence direction is outside the plane swept by the surface normal.

One additional mode of operation could be to keep the sample fixed in space and to sweep a small angle-resolving analyzer across the emission hemisphere. In fact, this measuring mode for intensity mapping has been successfully applied to Auger electron diffraction [17], and more recently also to Fermi surface mapping [12]. There is one principle difference between the fixed-crystal (which is present also for the display-type analyzer) and rotating crystal approaches: In the first case the light incidence is at a fixed angle relative to the crystal lattice, while in the second case it is at a fixed angle relative to the electron emission direction. In the latter case we expect the excitation matrix element to be constant for equivalent initial and final states, and the produced Fermi surface maps should thus present the full symmetry of the surface under study. As a matter of fact, if the light incidence is outside the plane swept by the surface normal (Fig. 7), mirror symmetries will be broken due to light polarization effects, as we shall see below. In the first case, with the light polarization residing fixed inside the crystal, very strong asymmetries are seen in the resulting images [11]. These asymmetries can provide information on the orbital character of the states on the Fermi surface, but they can also obscure its shape in unfavourable cases. Quite generally it can be said that any feature containing well-defined contours, regardless of their intensities, provides information on the location and shape of the Fermi surface. Caution is indicated if the used excitation radiation is not 'clean', i.e. if weak satellites produce additional weak contours that are associated with a different photon energy.

Three-dimensional Systems

Copper as a Test Case

The Fermi surface of Cu is maybe the best studied of all solids and its dimensions and shape are well known from dHvA experiments [1,18] (see Fig. 3). Also, from the point of view of the photoemission experiment, Cu has the advantage to produce clean and unreconstructed low-index surfaces after standard preparation techniques, which remain stable for extended periods of time under ultrahigh-vacuum conditions.

In Fig. 8a-c we present Fermi surface maps from three differently oriented Cu surfaces, all taken at a photon energy of 21.2 eV [8]. As expected, we observe sets of well-defined, continuous lines for all three cases. Fig. 9 illustrates, for one azimuthal trace of the measurement of Fig. 8b ($\theta_m=66°$), how these lines of high emission intensities are actually formed by direct transitions moving through the Fermi level: The fast-dispersing sp-band is occupied along the $[\bar{1}\bar{1}2]$ azimuth of the Cu(111) surface. Rotation away from this azimuth finds the transition moving towards E_F where it crosses at some azimuthal angle. If the DT peak in the energy spectrum were infinitely sharp, this crossing would produce an equally sharp intensity rise at the crossing angles. As can be seen in Fig. 9, the energy peaks are by no means sharp delta functions but they are broadened, in this case by limited angle- and energy resolution, or intrinsically by electron phonon, electron-defect and electron-electron scattering [19,20]. Consequently, the Fermi level crossings will have some width as a function of emission angle and thus in k-space. It is
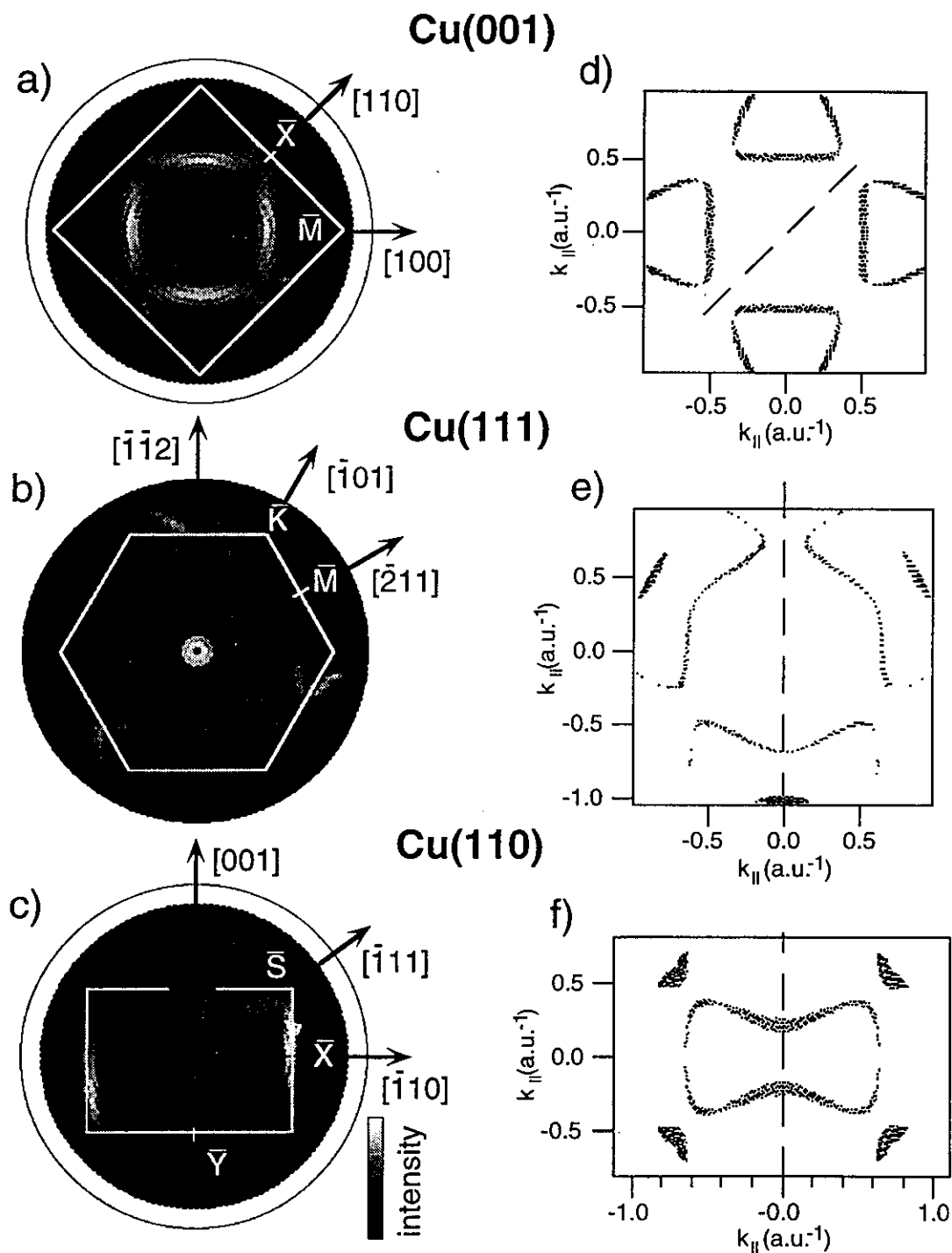
Fig. 8: Fermi surface maps from Cu(001) (a), Cu(111) (b) and Cu(110) (c). The different surface Brillouin zones (white lines) and high-symmetry points and directions are indicated. Normal emission is in the center of each figure. (d)-(f) Sections through the bulk Fermi surface using a free-electron final state (see text). The dashed lines represent the plane shown in Fig. 2.

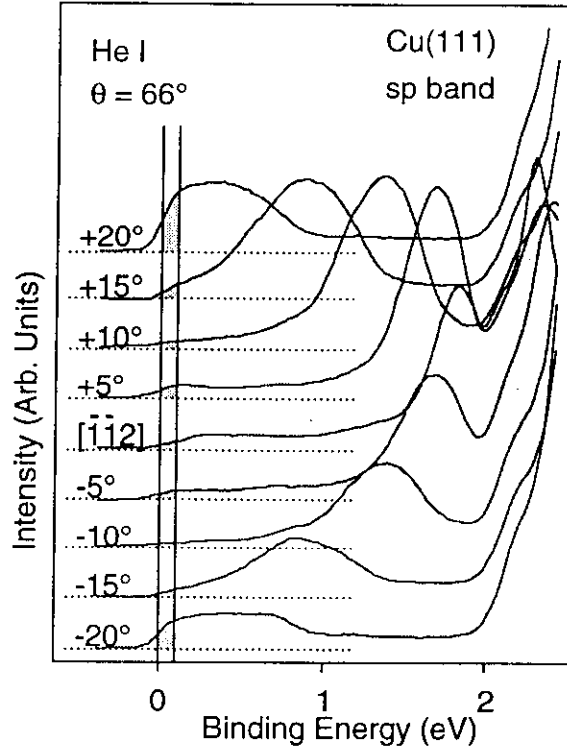clear that experimental energy- and angular resolution are intimately interconnected by the band structure E(**k**).

Fig. 9: HeI excited energy spectra from Cu(111) at a polar angle of 66°. Azimuthal angles around the [1̄1̄2] direction are indicated. Vertical lines limit the energy window applied to the angle scans of Fig. 8.

Now that we have seen the formation of Fermi contours we have to establish the precision and reliability with which the real Fermi surface is represented by these contours when using free-electron final states for data interpretation. To this purpose we give in Figs. 8d-f the results of a theoretical calculation for these same contours. A Fermi surface of Cu was calculated using the layer-Korringa-Kohn-Rostocker (LKKR) formalism, which is in good agreement with dHvA data. This Fermi surface was then intersected with the free-electron final-state sphere (the dashed lines indicate the (1̄10) plane of Fig. 2), which had previously been corrected for refraction effects (Fig. 4) in order to give a one-to-one comparison with the measured contours. In doing so, a value of 13.5 eV was taken for V_0 [21] and 4.7 eV for Φ. The agreement found in Fig. 8 for the main contours puts in evidence that this is a viable technique to obtain reliable Fermi surface information and that the free-electron final state approximation is a very good starting point for accurate 3D **k**-space mapping. It further appears that $k_\perp$ is relatively well-defined, otherwise the contours should be much more smeared out.

As mentioned earlier, photon polarization effects manifest themselves, for the given experimental configuration of Fig. 7, as asymmetries in contour intensities for **k**-points that are otherwise related to each other by mirror-symmetry operations. This phenomenon can be seen, e.g. in the data from the (111) surface (Fig. 8b), where the measurement touches the L-point necks
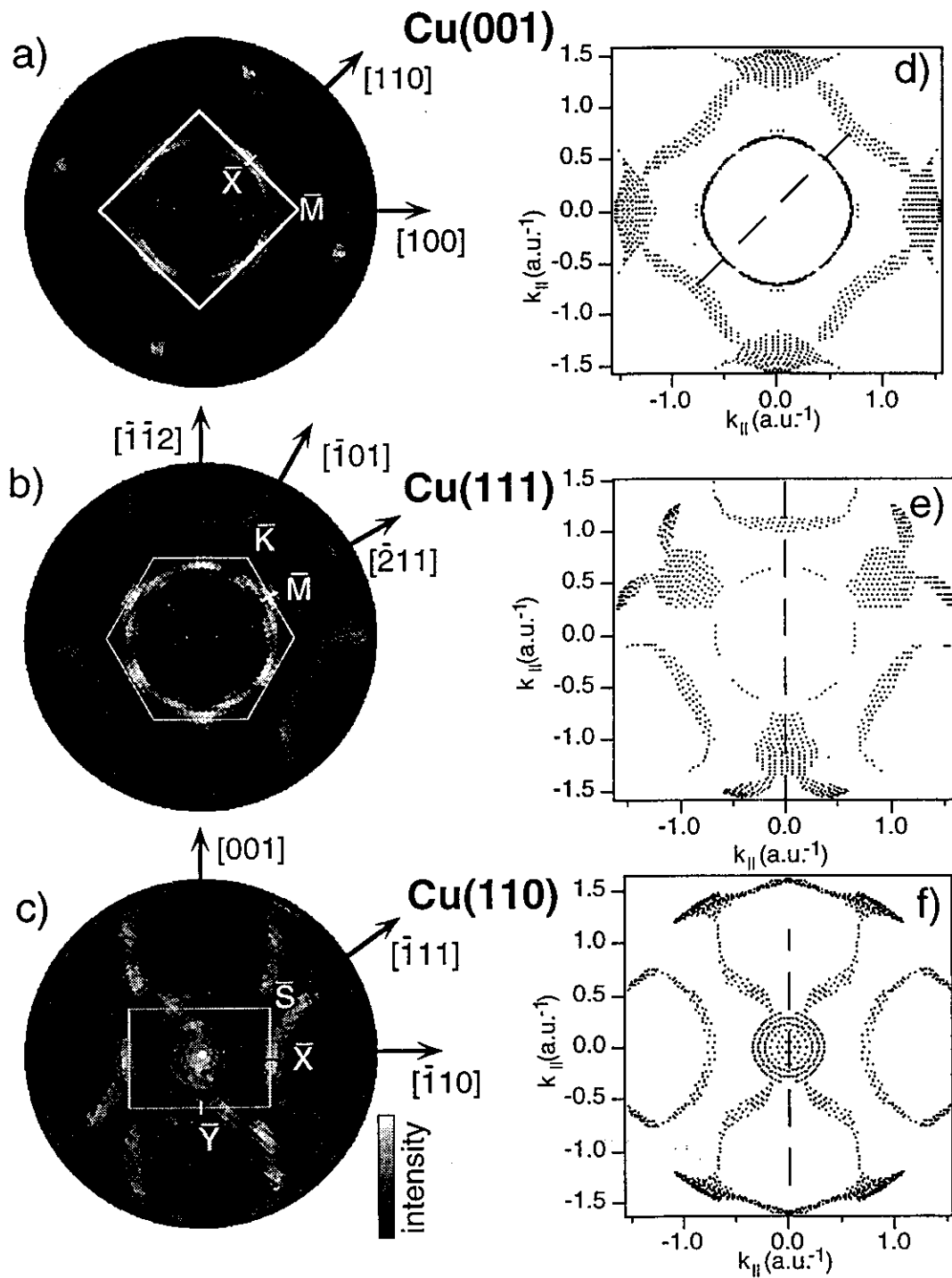
Cu(001)

a)

[110]

$\bar{X}$ $\bar{M}$

[100]

d)

1.5
1.0
0.5
$k_{\parallel}$ (a.u.$^{-1}$) 0.0
-0.5
-1.0
-1.5

-1.0   0.0   1.0
$k_{\parallel}$ (a.u.$^{-1}$)

[$\bar{1}\bar{1}2$]   [$\bar{1}01$]

b)

Cu(111)

[$\bar{2}11$]

$\bar{K}$

$\bar{M}$

e)

1.5
1.0
0.5
$k_{\parallel}$ (a.u.$^{-1}$) 0.0
-0.5
-1.0
-1.5

-1.0   0.0   1.0
$k_{\parallel}$ (a.u.$^{-1}$)

[001]

c)

Cu(110)

[$\bar{1}11$]

$\bar{S}$

$\bar{X}$

[$\bar{1}10$]

$\bar{Y}$

intensity

f)

1.5
1.0
0.5
$k_{\parallel}$ (a.u.$^{-1}$) 0.0
-0.5
-1.0
-1.5

-1.0   0.0   1.0
$k_{\parallel}$ (a.u.$^{-1}$)

Fig. 10: Same as Fig. 8 but for excitation with HeII radiation (40.8eV).

12

at three places. Each time the intensity on the clockwise side of the neck is significantly weaker than it is on the counter-clockwise side. Although the experiment has been carried out with unpolarized radiation, the oblique orientation of the photon incidence direction nevertheless means a tilt of the polarization plane with respect to the scattering plane, defined by the photoelectron emission direction and the surface normal. Clockwise rotation then moves the states near the neck further away from the polarization plane while the opposite sense moves them closer. Similar mirror-symmetry breaking effects have been observed in core-level photoelectron diffraction and Auger electron diffraction experiments [22].

Besides the main contours seen both in experiment and in theory, the measured images show additional structure. Most prominently, there is a very bright small ring in the center of the surface Brillouin zone of the Cu(111) surface (Fig. 8b), which is absent in the calculations (Fig. 8e). This feature can be identified with the well-known Shockley-type surface state [23]. It does not appear in the calculation which has been carried out considering bulk Bloch states only. Similar but much weaker surface state features are found near the $\overline{Y}$ point on the Cu(110) surface (see below). Additional structure can be found in the background region between the main contours. Some of this must be due to satellite contributions to the unmonochromatized HeI radiation, others due to nondirect transitions. In fact a small step at E_F can be seen for all angles in Fig. 9, also away from the Fermi level crossings of the sp band.

In Figs. 10a-c we give a similar presentation of measured FS contours from the same Cu surfaces, measured at a higher photon energy of 40.8 eV (HeII). The corresponding final-state sphere has been indicated in Fig. 2, and we give in Figs. 10d-f again the calculated contours from intersecting it with the Fermi surface. Again, excellent agreement is found. A wider region in k-space is accessible at this energy. Quite remarkably, in the Cu(110) measurement the final-state sphere touches the Fermi surface in normal emission, producing an extended circular region of higher intensity, modulated by matrix-element effects.

Nickel, a Magnetic Case

While the Fermi surface of Cu had been perfectly accessible with other techniques, Ni presents an interesting case where strong temperature effects are expected on the Fermi surface due to the phase transition from an itinerant ferromagnetic state below a critical temperature of T_c=631K to a paramagnetic state at higher temperatures. Clearly, dHvA or related experiments cannot be applied in this elevated temperature range as all scattering rates become prohibitively high. In such a situation, photoemission can play an important role in providing unique high-resolution Fermi surface information.

A section through the room temperature Fermi surface of Ni, as viewed through the (110) surface analogous to the situation shown in Fig. 2, is given in Fig. 11a [24]. Various pieces of Fermi surface are contained in this section. We illustrate two different procedures that can be applied to analyze such raw photoemission data when dealing with a less well-known Fermi surface as is
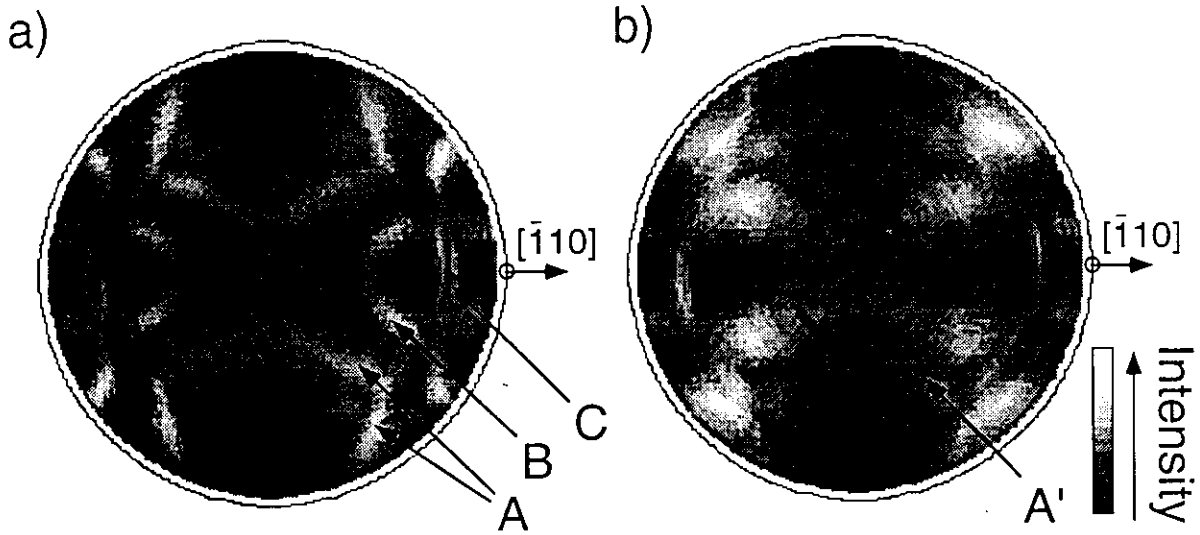
13

Fig. 11: (a) Room temperature Fermi surface map from Ni(110), excited with HeI radiation and using an energy window of 30meV centered at the Fermi energy. (b) Same as (a), but for a temperature of 700K which is above the critical temperature (631K) of ferromagnetic nickel. Several features are marked by capital letters in order to facilitate their discussion.

the case here. First we compare the experimental contours, like in the copper case, to calculated Fermi surface contours, now obtained using the spin-polarized LKKR formalism. In this case, Ni is in a ferromagnetic state and we have to consider the two spin systems separately. The majority-spin or spin-up system will have a Fermi surface composed of essentially sp-like states, because the d-shell is filled for electrons with their spins aligned parallel to the sample magnetization. This part of the Fermi surface is indicated by lightly shaded contours in Fig. 12a. The minority spin electrons contribute the darker shaded contours. Black regions correspond to k-locations where the two Fermi surfaces overlap. Comparing now Figs. 11a and 12a we find an
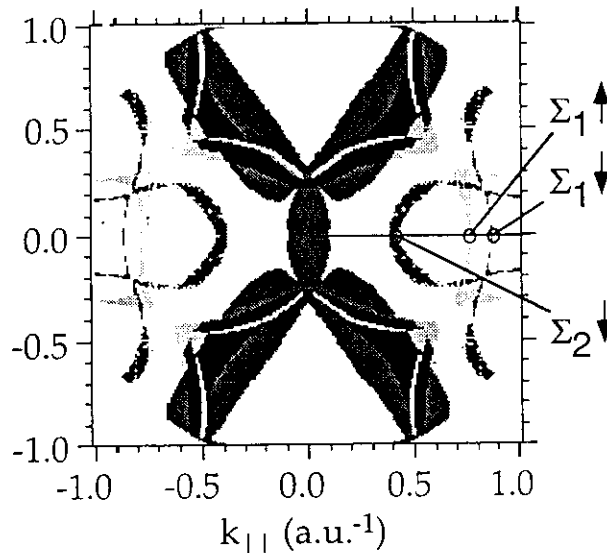

Fig. 12: Calculated section through the bulk Fermi surface of ferromagnetic nickel using the spin-polarized LKKR scheme for the initial state and a free-electron final state. Majority spins are given in light gray, minority spins in dark gray. Overlapping regions appear black.
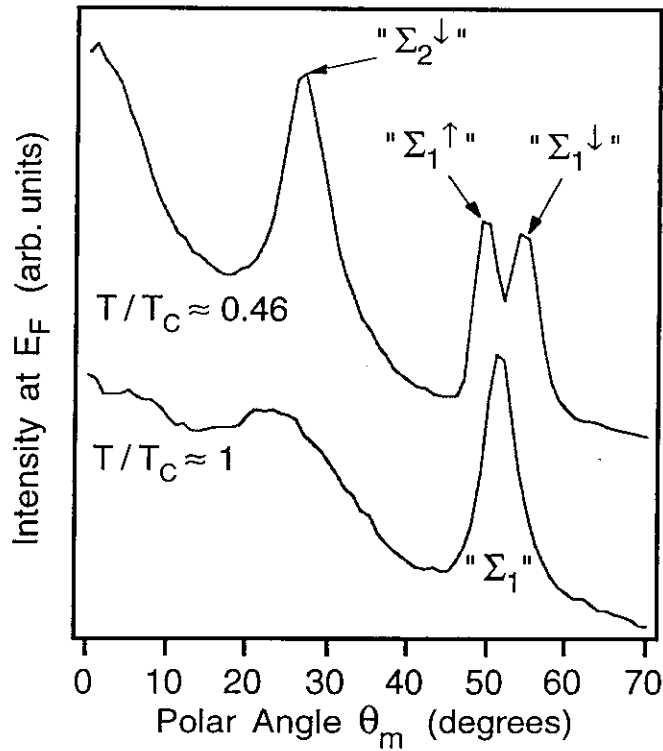
14

Fig. 13: (a) Polar section through the room temperature Fermi surface map of Fig. 11a along the [$\bar{1}10$] azimuth. (b) Same as (a) but for a temperature of 700K.

excellent agreement as to the positions of Fermi contours, thus providing us with a means for spin-assignment of the measured features. Even the fine splitting of minority and majority related contours labelled $\Sigma_1^{\downarrow}$ and $\Sigma_1^{\uparrow}$ in Fig. 12a, which are of sp-like origin as a band structure calculation [25] tells us, can be clearly seen in the experimental data (feature C). This splitting becomes much more apparent in a section through these data along the [$\bar{1}10$] azimuth (Fig. 13a): Two intensity maxima are well separated with angular positions of 54.5° and 49.5°. The strong arc-shaped feature B is of minority d-like origin, while for feature A no clear spin assignment can be given from this comparison.

An alternative method to analyze this sort of data is to compare quantitatively some Fermi surface locations to existing low-temperature dHvA measurements [26]. In order to do this, it is useful to project the measured Fermi surface sections, which intersect the final state sphere in the second Brillouin zone (Fig. 2), into the first zone. The procedure is as follows: Using Eqs. (6) and (7) for each intensity measurement $I(\theta_m, \phi_m)$ the corresponding k-point inside the solid is calculated. The nearest reciprocal lattice vector G is then determined and subsequently subtracted from this k-point, translating it into the first Brillouin zone. Fig. 14 shows the image produced that way in the first zone. The measured data set now lies on a series of four spherical sectors, each sphere centered at some reciprocal lattice vector. As before, intensities are given in a linear gray scale, producing bright contours where
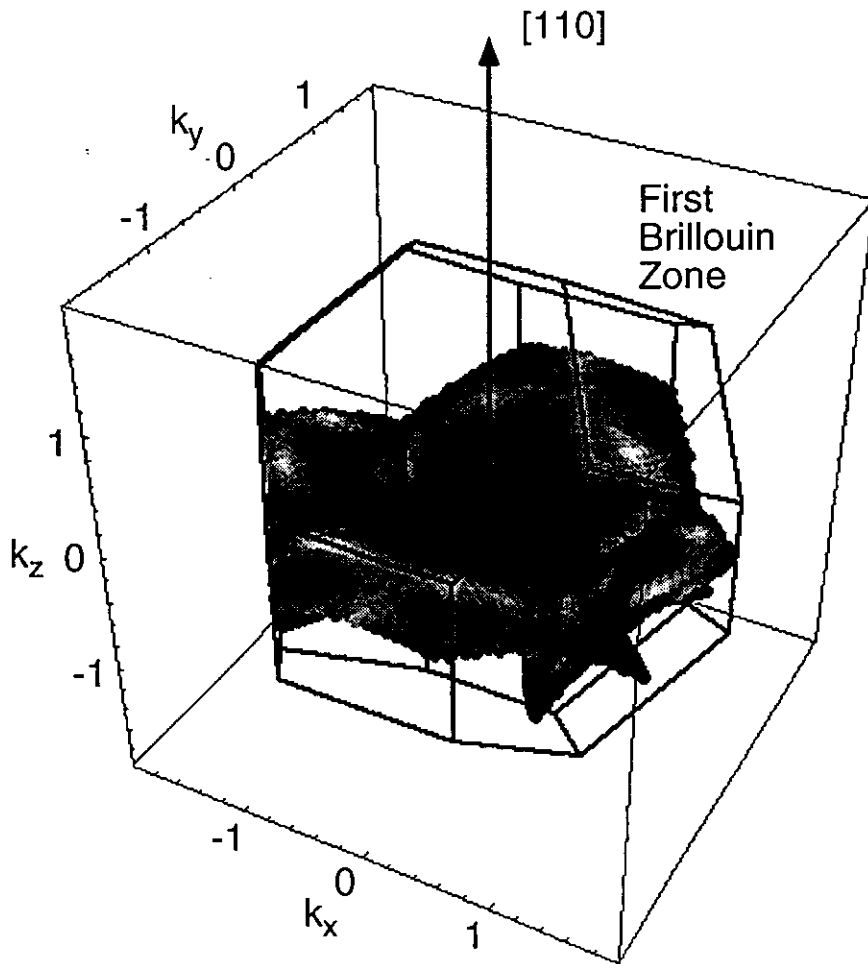
Fig. 14: 3D view of the Fermi surface map of Fig. 11a after projection into the first Brillouin zone. Note the reversed order in which the contours appear when moving from the zone center towards the boundaries as compared to Fig. 11a.
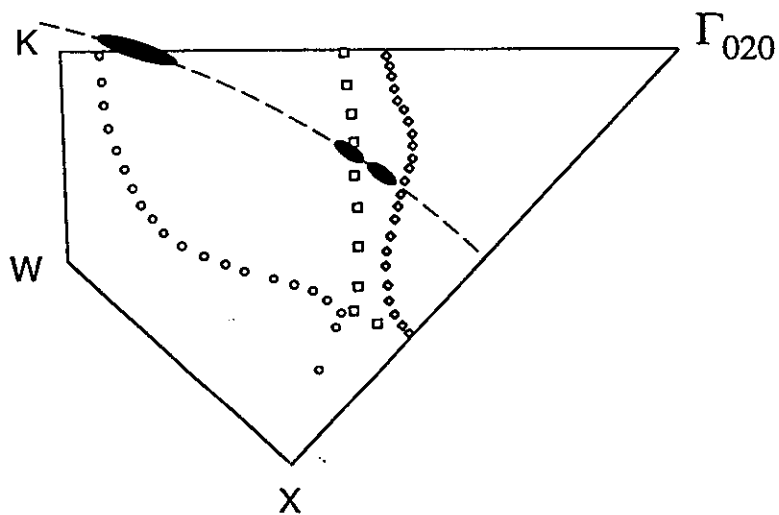

Fig. 15: Fermi surface cross sections of Ni in the (001) plane obtained from de-Haas-van-Alphen experiments (open symbols, from Ref. 26) compared to the data extracted from Fig. 14 (filled ellipses).

16

the measurement surface intersects the Fermi surface. Fig. 15 gives a section through this plot, showing one irreducible part of the Brillouin zone in the (001) plane. The measurement surface is indicated by the dashed circular line, Fermi surface intersections by black ovals. The dHvA data [26] are given by open symbols. We find rather good, though not fully quantitative agreement between the two techniques. Small deviations may arise due to the use of the free-electron final-state model, or maybe just because the two measurements were carried out at different temperatures. In any case this figure indicates the sort of accuracy that can be expected from these experiments given this simple level of interpretation.

Apart from these possible systematic deviations due to this final-state approximation we would like to discuss the question of k-space resolution. The measured Fermi surface locations are given by black ovals of a size that represents the angular width of the corresponding contour in the measurement. As can be seen from Fig. 13, the two sp-band transitions are significantly sharper than the minority d-band transition ($\Sigma_2^{\downarrow}$). This difference may be attributed to the more grazing emission angles of the first two transitions. As mentioned earlier, there is some smearing out associated with $k_{\perp}$ and essentially none with $k_{\parallel}$. Consequently, the more weight $k_{\parallel}$ has at a particular measuring angle, the better that particular k-point is defined. This means that different sections of a Fermi surface can be measured with varying precision, depending on the crystal face of the solid one chooses for the photoemission experiment. One should also not forget that the group velocities of the initial state bands will play a role in the measured contour width. For a flat band like the minority d-band a certain energy spread in the detector window will cause a larger k-smearing than for the steeper sp band [19].

We now discuss the changes in the Fermi surface contours as the temperature is raised slightly above the critical point. Without entering much into the ongoing debate about the behaviour of the exchange splitting between the two spin subbands, the intensity-versus-angle sections given in Fig. 13 show that the minority and majority contours associated with sp-band emission coalesce near the critical temperature but remain otherwise as a well-defined feature in the Fermi contour plot of Fig. 11b. The minority d-band related features A and B appear to merge, forming a rather extended region of high intensity in between them. There are two physical explanations for the occurrence of such bright regions. A first one we have encountered in the HeII-excited data from Cu(110) (Figs. 2, 10c, f): When the measuring sphere touches the Fermi surface glancingly, the direct transition condition is fulfilled for many k-locations in an extended region. A similar situation can arise in situations with a very flat band, and thus a high density of states very near to the Fermi energy. It is not clear which of these two mechanisms is involved in the present case. Closer inspection of this region indicates, however, that some parts of the room-temperature Fermi surface remain visible (feature A'), indicating at least partly the coexistence of spin-polarized and paramagnetic bands in these Fermi surface contours above T_c. The significance of the kind of data presented here is that the information is on the Fermi surface directly, which should be closely linked with the driving force for the magnetic phase transition. In conjunction with theoretical models describing the temperature-dependent evolution of the band structure these data should serve as an

important benchmark, in addition to providing some intuitive idea as to the behaviour of the various bands over an extended region in **k**-space.

Two-dimensional Systems

$Bi_2Sr_2CaCu_2O_{8+\delta}$ High-Temperature Superconductor

Before addressing truly surface-related Fermi surface contours we give a brief description of our experiments on cuprate high-temperature superconductors [9,27] which represent quasi-2D systems as far as the relevant electronic bands near the Fermi surface are concerned. $Bi_2Sr_2CaCu_2O_{8+\delta}$ crystals have a layered structure of alternating metal-oxide planes [28]. They cleave nicely between two Van-der-Waals-bonded Bi-O planes. The bands forming the Fermi surface are constituted by states that are located on the two Cu-O planes separated by Ca atoms, and they are known to be essentially two-dimensional [29].

Fermi surface contours have been constructed by Dessau et al. [30] by tracing, for various azimuthal directions ϕ_m, $k_{||}$-locations where a dispersing peak crosses the Fermi level. This procedure relies on a detailed line shape analysis of the spectra near E_F. In these strongly correlated systems where the photoemission signal is composed of a dispersing quasiparticle peak and a large incoherent background, finding the exact crossing point is no simple task. We have therefore conducted Fermi-surface mapping experiments on such samples. Complementary to the experiments by Dessau et al. [30], this approach relies on the measurement of the absolute intensities at E_F, a quantity which is not exploited in the other approach. Fig. 16a shows the resulting intensity map. In order to enhance weaker features, intensities are here translated logarithmically into gray levels. Well-defined continuous lines are observed, with some minor but significant deviations from the result of Dessau et al.. A Fermi surface calculation [29] for this same material (Fig. 16d) agrees very well with the most prominent subset of contours seen in the data. Specifically, the general shape of the Fermi surface is well reproduced in the calculation, and the position of the Fermi wave vector along the ΓX-direction is quite accurate. On the other hand, the small circular contour half-way between Γ and Z, which the calculation attributes to hole pockets associated with the Bi-O planes, is not seen in the data. Whether it is not present in the bulk electronic structure of $Bi_2Sr_2CaCu_2O_{8+\delta}$, or whether it is solely absent in the surface-layer Bi-O plane, this question cannot be resolved by this experiment. The first bulk-like Bi-O plane is buried about 13 Å below the surface and hardly contributes to the measured photoemission intensities. Moreover, in the calculation two Cu-O bands contribute to the Fermi surface, leading to the split contours, especially around the Z point. Experimentally we find that the measured contours have a full width at half maximum in $k_{||}$ of the order of 0.1 Å^{-1} which is just about the maximum separation of the two bands at the Fermi level and which can thus hardly be resolved. We are here not limited by the angular or energy resolution of the experiment but by the intrinsic width of the features.

In addition to these strong Fermi surface contours we observe also additional features, some of which are due to a c(2x2) superstructure on the
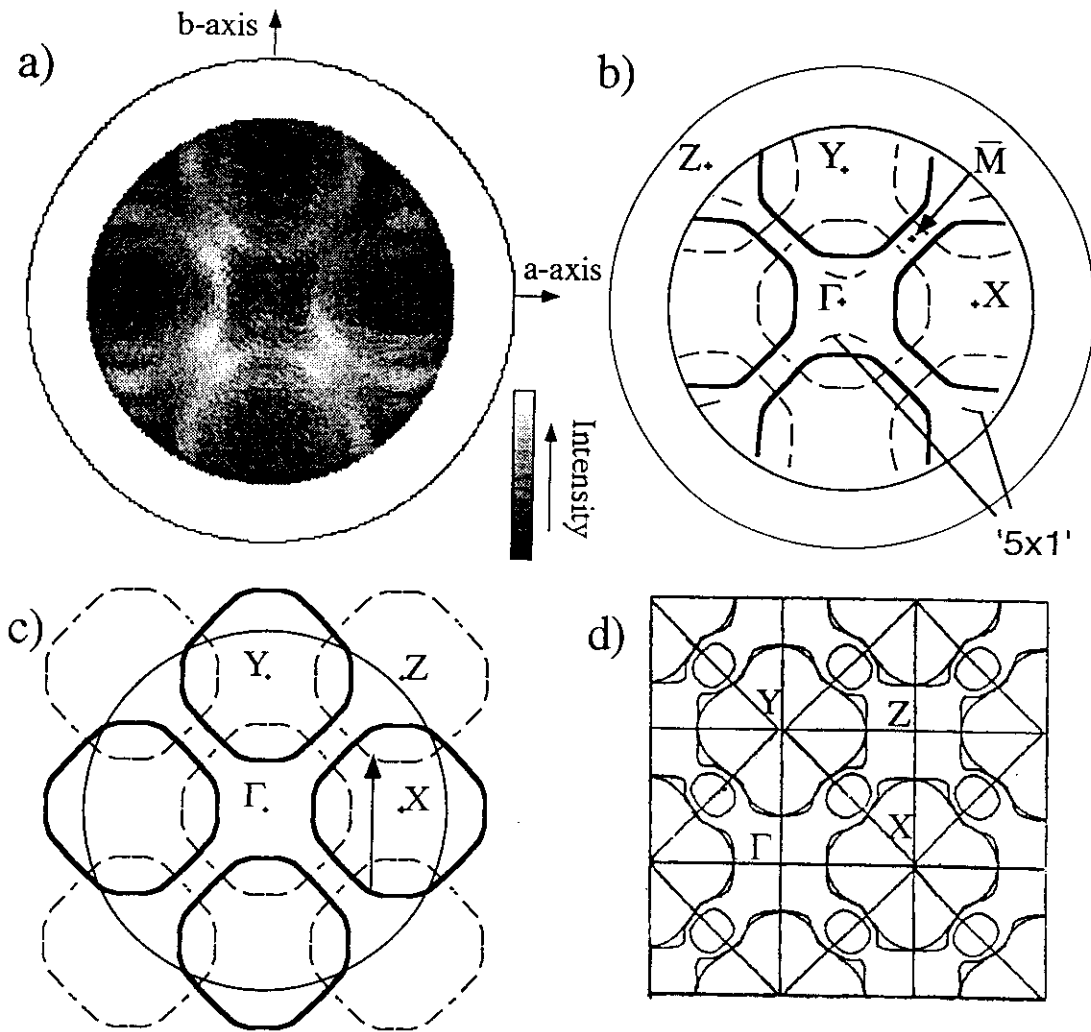
Fig. 16: (a) Fermi surface mapping of $Bi_2Sr_2CaCu_2O_{8+\delta}(001)$ using an energy window of 30meV, centered at E_F. A logarithmic intensity scale is used for gray levels in order to enhance weaker features. (b) Outline of (a), emphasizing the fine lines observed in the measurement and distinguishing between the stronger (thick lines) and weaker (dashed lines) sets of contours. (c) This drawing shows how these lines have the symmetry of a c(2x2) superstructure. (d) For comparison, the calculated Fermi surface for this compound from Ref. 29.

Fermi surface [9] (dashed lines in Fig. 16c) and others due to the quasi-(5x1) incommensurate lattice modulation [27] which is a structural peculiarity of these Bi cuprates. The observation of such superstructures may be important in understanding the normal-state electronic structure of these materials and shall not be discussed at this place. We emphasize, however, that these features had not been seen experimentally before, and that the visualization of photoemission intensities in this 2D fashion greatly enhances the sensitivity to weak extra features.

In the discussion of the Cu bulk Fermi surface mapping we have already pointed out that a surface state appears in the center of the surface Brillouin zone on the (111) surface (Fig. 8b). In Fig. 17a we give a higher-resolution map of this surface state, displaying clearly the free-electron-like circular shape. A polar section through these data shows the high signal-to-background ratio and the narrow width of the surface Fermi-surface contour, which is less than 3° full width at half maximum. The existance of this surface state is closely related to the gap in the surface-projected band structure associated with the necks around the L points. Similar gaps in $k_{||}$ exist also on the (110) surface, and a surface state has also been observed here [31]. Fig. 17c gives a nice view on how this surface state, also rather circular in shape,
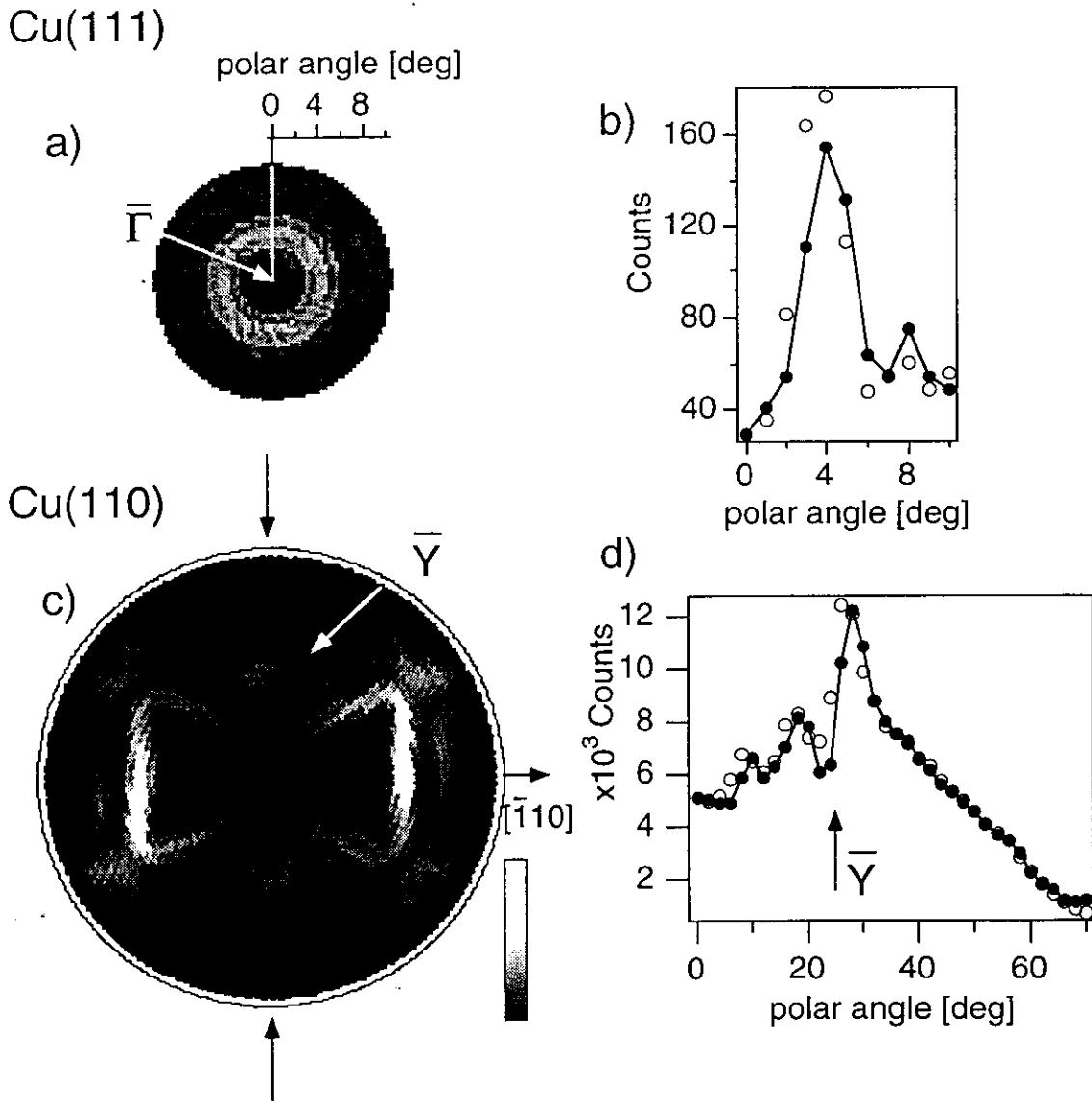

Fig. 17: (a) High-resolution map (more than 2000 angular settings) of Fermi level intensities near the center of the surface Brillouin zone of Cu(111), showing the Shockley surface state. (b) Two polar sections through these data (open and closed circles) spaced by 180° in azimuth. (c) Fermi surface map from Cu(110) indicating the surface state centered at the $\overline{Y}$ point. (d) Sections through the data of (c) along the azimuths indicated by black arrows.

is situated relative to the bulk Fermi surface contours. If one considers the projected band structure more closely, one finds that this state has already moved out of the projected band gap by the time it reaches the Fermi energy [31], at least along the $\overline{\Gamma Y}$ direction. Strictly speaking, the circular Fermi contours are thus associated with a surface resonance rather than with a true surface state. Translational symmetry within the (110) surface demands that this circle be centered precisely on the zone boundary. From this condition we can verify independently the accuracy of our k-space mapping procedure. We know the exact location of the $\overline{Y}$ point relative to the $\overline{\Gamma}$ point, the distance being $\overline{\Gamma Y} = \pi / a_0 = 0.87\text{Å}^{-1}$ (a_0=3.61Å). From Eqs. (3) and (5) we obtain the relation

$$k_\| = \frac{1}{\hbar}\sqrt{2m(h\nu - \Phi)}\sin\theta_m = \overline{\Gamma Y}. \qquad (8)$$

Taking the well-established work function value of 4.48eV for Cu(110) obtained from photoemission cutoff measurements [32], we arrive at a polar angle of θ_m=24.5° for $\overline{Y}$. Fig. 17d, providing a polar section along the $\overline{\Gamma Y}$ direction, indicates that we ovserve the center of the surface state at a slightly smaller polar angle of 22±1°.

sp Surface State on Al(001)

A similar sp-derived surface state has been observed on Al(001) [33]. In this case the maximum binding energy is 2.75eV while it was only 0.4eV in the case of the Cu sp surface states. Its Fermi surface will therefore cover a much larger area in $k_\|$, and it should be interesting to see how it interacts with various bulk bands. Fig. 18 shows the highly parabolic dispersion of this state, which can be well fitted with an effective mass of m^*=1.18m_e, in excellent agreement with earlier data [33,34]. This plot represents a series of spectra
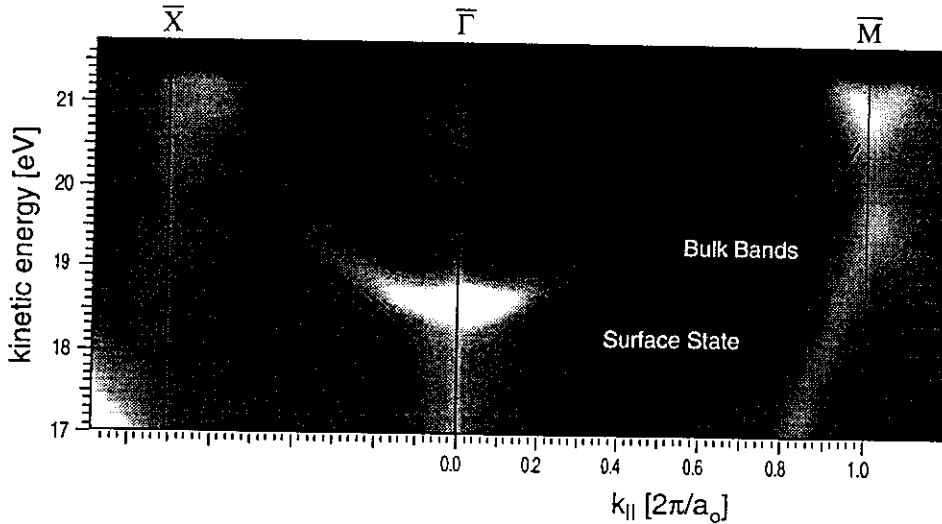

Fig. 18: Series of energy spectra from clean Al(001), representing polar scans along the [100] azimuth ($\overline{\Gamma M}$) and the [110] azimuth ($\overline{\Gamma X}$). The presentation is in a linear gray scale with low intensities in black and high intensities in white. Surface and bulk transitions are indicated.

measured on a dense grid of polar angles along the $\overline{\Gamma X}$ and $\overline{\Gamma M}$ directions which have been mapped onto $k_\parallel$ according to

$$k_\parallel = \frac{1}{\hbar}\sqrt{2m(h\nu - E_B - \Phi)}\sin\theta_m.\qquad(9)$$

where E_B is the measured binding energy within the spectra. Intensities are given in a linear gray scale much like it is done in the Fermi surface maps, providing a very direct representation of the dispersion [35]. Even though emission from the surface state becomes rather weak away from the $\overline{\Gamma}$ point, this sort of plot permits a clear tracing of the dispersion and of the Fermi level crossing which occurs at 0.60 in units of $2\pi/a_0$.
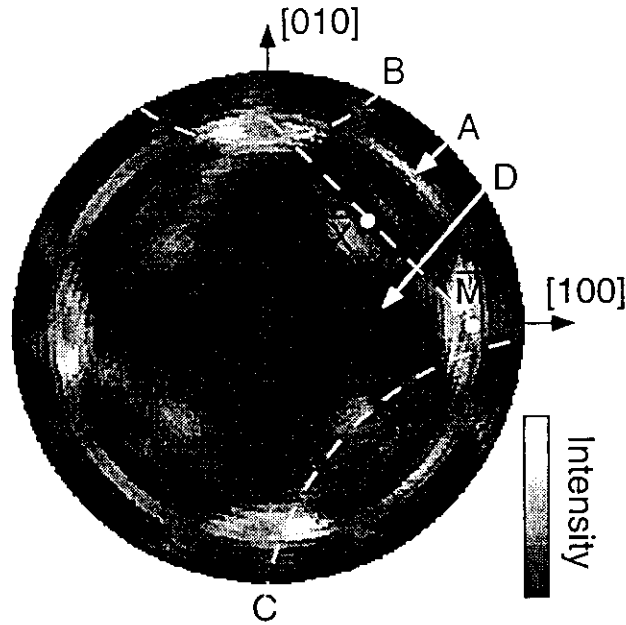

Fig. 19: Fermi surface map from clean Al(001). Several features are emphasized by dashed curves in one of the four symmetry-equivalent places and marked by capital letters. The boundary of the surface Brillouin zone is given at one place by the straight dashed line.

A Fermi surface map is given in Fig. 19, measured with He I radiation. While the Fermi contours are here much more complex than in Cu, an intuitive understanding of all features is still possible within the simple framework discussed earlier. Fig. 20 gives a schematic view of the situation in k-space, along the $\overline{\Gamma M}$ direction, i.e. within the (100) plane. A simplified free-electron Fermi surface for Al is plotted centered about four reciprocal lattice points which are relevant for this geometry. We neglect here the effects of the lattice potential on the Fermi surface since we just want to be able to give an assignment to the various measured contours. Like in Fig. 2 a free-electron final state for excitation with He I radiation is also given, which reaches here further out due to the smaller Brillouin zone dimensions in Al as compared to
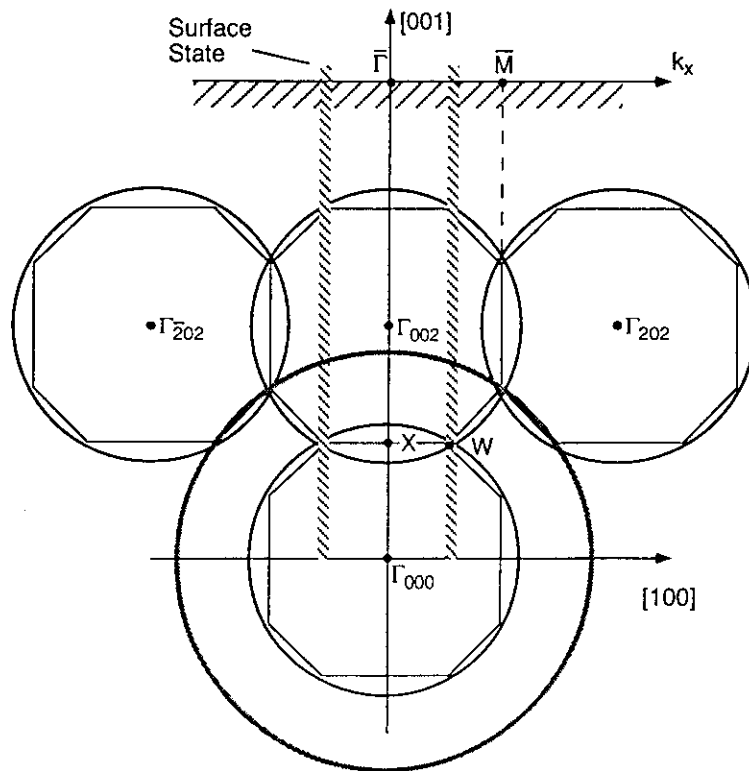
Fig. 20: Section through the reciprocal lattice of Al parallel to the (010) plane, analogous to Fig. 2. The bulk Brillouin zones are given by the polygons and the idealized free-electron Fermi surface of Al is drawn around four reciprocal lattice points. The large circle represents the final states for HeI excitation. The location of the surface state is indicated by the hatched bars.

Cu. We can immediately understand now the large circular contour A in the data as being due to the intersection with the Γ_{020} - centered Fermi sphere. The Γ_{022} spheres give rise to the arc-shaped contours B, while the Γ_{111} spheres (not shown in Fig. 20) produce the four symmetry-related arcs C. Most of the observed contours are readily accounted for in this simple picture. The surface state appears as a weak circular contour D touching the bulk bands in the $\overline{\Gamma X}$ directions. The corresponding regions of $k_{||}$ are indicated in Fig. 20. This figure suggests that the state might actually be associated with a small gap at the W-points and thus be a true surface state even at the Fermi energy. In other directions, especially along $\overline{\Gamma X}$, the $k_{||}$ values would pass near the U-points of the bulk Brillouin zone where there is no gap at E_F. This contour D comprises thus both true surface states and surface resonances.

23

Conclusions and Outlook

The examples presented in these notes demonstrate that this new approach to the photoemission experiment provides a very powerful tool for mapping Fermi surfaces directly. It can be applied to any material that can be prepared in single-crystalline form of a few mm^2 surface area and thickness down to atomic monolayers. 3D and 2D systems can be measured. given the wide-open parameter space accessible by photoemission experiments (temperature, concentrations, film thickness, dimension (2D -> 3D), etc.) this technique should be particularly useful to study phase transitions and their interrelation with the Fermi surface [36].

While the positions of the Fermi surface contours are well explained within the simple free-electron final state model, there is now also a growing understanding of the intensity variations along the contours. A more sophisticated final state wave function is needed here, which takes into account the angular momentum character of the photoelectron wave and the elastic scattering within the surface region [7,37,38]. Finally, the analysis of the widths of such contours might be of considerable interest in studying low-energy excitations in correlated systems. The analysis of line widths in energy spectra have attracted a great deal of attention in this context [19]. Very recently we have shown that in momentum space such line widths can be extracted more precisely due to a simpler line shape and a better-defined background [39,40]. It should be mentioned that other constant-energy surfaces below the Fermi surface can be measured equally well such that all the studies discussed here can be extended to higher binding energies [27,41].

References

[1]   N. W. Ashcroft, N. D. Mermin, *Solid State Physics* (Holt, Rinehart and Winston, New York 1976).
[2]   R. Ribberfors, Phys. Rev. B **12**, 3136 (1975).
[3]   S. Berko, in *Momentum Densities*, eds. R. N. Silver and P. E. Sokol (Plenum 1989).
[4]   S. Hüfner, *Photoelectron Spectroscopy* (Springer, Berlin 1995).
[5]   R. H. Gaylord, K. Jeong, and S. D. Kevan, Phys. Rev. Lett. **62**, 203 (1989).
[6]   A. Santoni, L. J. Terminello, F. J. Himpsel, T. Takahashi, Appl. Phys. **A52**, 229 (1991)
[7]   J. Osterwalder, A. Stuck, T. Greber, P. Aebi, L. Schlapbach, S. Hüfner, in *Proceedings of the 10th Vacuum Ultraviolet Radiation Physics*, F. J. Wuilleumier, Y. Petroff, I. Nenner eds., (World Scientific, Singapore 1993), p. 475.
[8]   P. Aebi, J. Osterwalder, R. Fasel, D. Naumovic, L. Schlapbach, Surf. Sci. **307-309**, 917 (1994).
[9]   P. Aebi, J. Osterwalder, P. Schwaller, L. Schlapbach, M. Shimoda, T. Mochiku, K. Kadowaki, Phys. Rev. Lett. **72**, 2757 (1994).
[10]   R. Leckey, J. Riley, Aust. J. Phys. **48**, 217 (1995).
[11]   Zhe Qu, A. Goonewardene, K. Subramanian, J. Karunamuni, N. Mainkar, L. Ye, R. L. Stockbauer, R. L. Kurtz, Surf. Sci. 324, 133 (1995).
[12]   J. Avila, C. Casado, M. C. Asensio, J. L. Perez, M. C. Munoz, and F. Soria, J. Vac. Sci. Technol. **A13**, 1501 (1995).
[13]   S. Doniach, Phys. Rev. B 2, 3898 (1970); N. J. Shevchik, Phys. Rev. B **16**, 3428 (1977).
[14]   D. E. Eastman, J. J. Donelon, C. Hien, and F. J. Himpsel, Nucl. Instrum. Methods **172**, 327 (1980).
[15]   J. Osterwalder, T. Greber, A. Stuck, and L. Schlapbach, Phys. Rev. B **44**, 13764 (1991).

[16]   R. Fasel and J. Osterwalder, Surf. Rev. Lett. **2**, 359 (1995).

[17]   D. G. Frank, N. Battina, R. Golden, F. Lu, and A. t. Hubbard, Science **247**, 182 (1990).

[18]   D. Shoenberg and D. J. Roaf, Phil. Trans. Roy. Soc. **225**, 85 (1962).

[19]   N. V. Smith, P. Thiry, and Y. Petroff, Phys. Rev. B **47**, 15476 (1993).

[20]   B. A. McDougall, T. Balasubramanian, and E. Jensen, Phys. Rev. B **51**, 13891 (1995).

[21]   J. B. Pendry, *Low Energy Electron Diffraction* (Academic Press, London 1974) p. 23.

[22]   T. Greber, J. Osterwalder, S. Hüfner, and L. Schlapbach, Phys. Rev. B **45**, 4540 (1992).

[23]   P. O. Gartland and B. J. Slagsvold, Phys. Rev. B **12**, 4047 (1975).

[24]   P. Aebi, T. J. Kreutz, J. Osterwalder, R. Fasel, P. Schwaller, and L. Schlapbach, submitted.

[25]   H. Eckardt and L. Fritsche, J. Phys. F **17**, 925 (1987).

[26]   unpublished results of Stark, see C. S. Wand and J. Callaway, Phys. Rev. B **9**, 4897 (1974).

[27]   J. Osterwalder, P. Aebi, P. Schwaller, L. Schlapbach, M. Shimoda, T. Mochiku, and K. Kadowaki, Appl. Phys. **A60**, 247 (1995).

[28]   A. Yamamoto, M. Onoda, E. Takayama-Muromachi, F. Izumi, T. Ishigaki, and H. Asano, Phys. Rev. B **42**, 4228 (1990).

[29]   S. Massidda, Jaejun Yu, and A. J. Freeman, Physica (Amsterdam) **158C**, 251 (1988).

[30]   D. S. Dessau, Z.-X. Shen, D. M. King, D. S. Marshall, L. W. Lombardo, P. H. Dickinson, A. G. Loeser, J. DiCarlo, C.-H. Park, A. Kapitulnik, and W. E. Spicer, Phys. Rev. Lett. **71**, 2781 (1993).

[31]   P. Heimann, J. Hermanson, H. Miosga, and H. Neddermeyer, surf. Sci. **85**, 263 (1979).

[32]   *CRC Handbook of Chemistry and Physics,* eds. R. C. Weast and M. J. Astle (CRC Press, Boca Raton 1980) p. E-82.

[33]   P. O. Gartland and B. J. Slagsvold, Solid State Commun. **25**, 489 (1978); G. V. Hansson and S. A. Flodstrom, Phys. Rev. B **18**, 1562 (1978).

[34]   H. J. Levinson, F. Greuter, and E. W. Plummer, Phys. Rev. B **27**, 727 (1983).

[35]   R. Fasel et al., in preparation.

[36]   S. D. Kevan, Surf. Sci. **307-309**, 832 (1994).

[37]   E. L. Shirley, L. J. Terminello, A. Santoni, and F. J. Himpsel, Phys. Rev. B **51**, 13614 (1995).

[38]   H. Daimon, S. Imada, H. Nishimoto, and S. Suga, J. Electron Spectrosc. Relat. Phenom., to appear.

[39]   T. J. Kreutz, P. Aebi, and J. Osterwalder, Solid. State Commun. **96**, 339 (1995).

[40]   P. Schwaller, P. Aebi, H. Berger, C. Beeli, J. Osterwalder, and L. Schlapbach, J. Electron Spectrosc. Relat. Phenom., to appear.

[41]   T. J. Kreutz, P. Aebi, J. Osterwalder, and L. Schlapbach, J. Electron Spectrosc. Relat. Phenom., to appear.